

Article

Novel High-Step-Up/Step-Down Three-Port Bidirectional DC/DC Converter for Photovoltaic Systems

Yu-En Wu 

Department of Electronic Engineering, National Kaohsiung University of Science and Technology, Kaohsiung 82401, Taiwan; yew@nkust.edu.tw; Tel.: +886-7601-1000 (ext. 32511)

Abstract: This paper presents a novel three-port high-step-up/step-down bidirectional DC/DC converter with a coupled inductor for photovoltaic (PV) systems. The proposed converter combines a high-step-up converter, which is used to step-up the PV module to DC bus 200 V, and a battery charge/discharge bidirectional converter to form a three-port bidirectional converter. When sufficient energy is supplied from the PV modules, the converter can step-up the output of the PV modules and provide energy to the DC bus while charging the battery simultaneously. However, when no energy is supplied from the PV modules, the DC bus voltage is provided by the battery. Moreover, the energy stored in the leakage inductor is recycled to the DC-blocking capacitor, and synchronous rectification is conducted in the switch during the step-up mode to reduce switch loss and thereby increase the system's overall efficiency. Finally, a 500 W three-port bidirectional converter is implemented to verify the feasibility and practicability of the proposed converter. The maximum efficiency of the proposed converter is 95.4%, 94.3%, and 94.7% when operated in the high-step-up mode, battery step-up mode, and step-down mode for the PV modules, respectively.

Keywords: three-port bidirectional converter; coupled inductor; photovoltaic system



Citation: Wu, Y.-E. Novel High-Step-Up/Step-Down Three-Port Bidirectional DC/DC Converter for Photovoltaic Systems. *Energies* **2022**, *15*, 5257. <https://doi.org/10.3390/en15145257>

Academic Editors: Tibor Vince and Dobroslav Kovac

Received: 1 June 2022

Accepted: 18 July 2022

Published: 20 July 2022

Publisher's Note: MDPI stays neutral with regard to jurisdictional claims in published maps and institutional affiliations.



Copyright: © 2022 by the author. Licensee MDPI, Basel, Switzerland. This article is an open access article distributed under the terms and conditions of the Creative Commons Attribution (CC BY) license (<https://creativecommons.org/licenses/by/4.0/>).

1. Introduction

In recent years, with the technological advances, the amount of greenhouse gas emission has been continuously increasing, leading to global warming and climate change. Our energy technology industry still relies heavily on fossil fuels and has been unable to handle the current stringent environment [1,2]. Therefore, the use of green energy has become the core economic strategy and is trending at the world politics, because the reduction in greenhouse gas emission and energy conservation are currently the major concerns worldwide.

In general, because of the large difference between the output voltage of green energy and the operating voltage of the DC bus, a high-step-up converter is always required for achieving these requirements. However, a conventional boost converter must operate at an extremely high duty ratio to meet the high-step-up voltage demand; moreover, the maximum step-up ratio is limited by the parasitic elements on the circuit's components. The existence of the parasitic components [3] and the reverse-recovery time of the diode [4] further reduce the converter's efficiency. These conditions have limited the use of a conventional boost converter in the field of green energy. Recently, the techniques of the series boost converter, voltage-lift, coupled inductor, and cascade circuit structure have been proposed to achieve a high-step-up ratio [5–12]. When the switch is open, a high current spike flows through the power components; therefore, power components with high current stress are required, thus increasing the costs and conduction energy loss. The conventional flyback converter and forward converter are also suitable for use in high-step-up converters. However, the leakage inductance of the transformer in these converters can cause a high reverse voltage on the switch, and therefore, either a passive snubber circuit or an active clamp is always required to suppress this reverse voltage. A passive snubber

circuit uses resistance to deplete the excess energy in the leakage inductor, thereby reducing the circuit efficiency.

An application block diagram of a typical green energy system is shown in Figure 1. While low cost, small circuit size, and high efficiency have been the objectives of R&D, energy storage is also a major research direction in the application of green energy. In a system working on a battery, a high-step-up converter that transfers energy from the battery to the DC bus is necessary due to the large voltage difference between the battery and DC bus. Recently, many studies have investigated bidirectional converters [13–22], a topology that can operate both step-up and step-down functions, which further reduces the number of components, cost, and size of the system. In a nonisolated bidirectional DC/DC converter with ZVS technology [13], ZVS is achieved using synchronous rectification technology and a clamping circuit, but the converter does not apply galvanic isolation. A switched-quasi-Z-source nonisolated bidirectional DC/DC converter [14] has a wide voltage gain range in step-up and step-down modes. However, all switches of this converter perform hard switching, which causes high switching loss. An isolated bidirectional Cuk topology [15] is suitable for photovoltaic (PV) applications. However, the high-voltage stress and high-current stress across switches can damage the circuit. Furthermore, these nonisolated circuits can be interfered with easily and cannot be used for electricity isolation; these factors considerably limit their usage. The commonly used isolated bidirectional converters include the full-bridge bidirectional converter [17], half-bridge bidirectional converter [19], and bidirectional flyback converter [18]. Both full- and half-bridge bidirectional converters can perform soft-switching by controlling the phase shift, which leads to high efficiency, but their designed transformers face difficulties in achieving LLC resonance. Moreover, the bidirectional flyback converter has the common advantages of few components, low cost, and easy design. When it is switched OFF, the leakage inductance of the transformer leads to resonance with the parasitic capacitor within the switch and causes a voltage spike at the switch; therefore, a switch with high-voltage stress is usually required. These isolated bidirectional converters typically possess a large-sized transformer because of the high turns ratio when operated at a high voltage conversion ratio. Recently, many modified bidirectional converters have been proposed. For example, [21] recycled the energy stored in the leakage inductor of the transformer and performed synchronous rectification, which led to high efficiency while meeting the requirement of electricity isolation. However, in the case of an ideal transformer, this converter topology requires two inductors. Despite having a lower turns ratio, the energy releasing problem for the magnetizing inductor causes low efficiency when operated at high power. In addition, [22] proposed the concept of charging the battery auxiliary power and providing energy for the DC bus during a circuit operating in the step-up mode. The leakage inductance of the coupled inductor can recycle the energy and release it to the circuit of the battery auxiliary power and DC bus on the high-voltage side. However, the control procedure is more complicated and the battery auxiliary power is unable to supply energy to the DC bus.

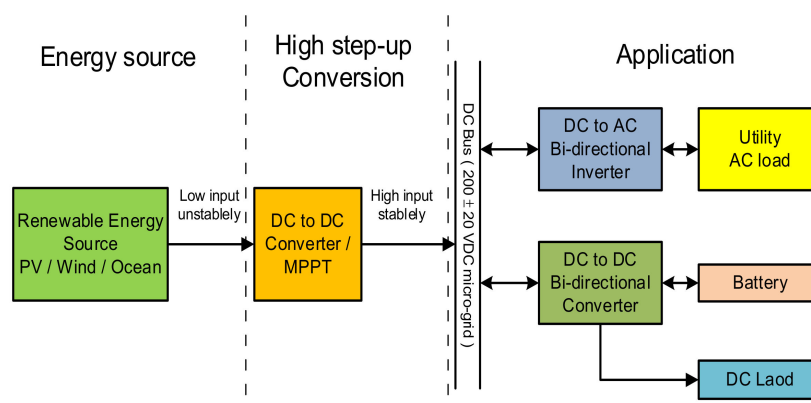


Figure 1. Application block diagram of green energy system.

Although a bidirectional converter combines the functions of step-up and step-down voltages, if it is applied to a PV system, the energy generated from the PV system must pass through two converter stages to charge the battery, thus reducing the overall system efficiency. To solve this problem, the topology of a three-port DC/DC converter has been proposed in the literature [23–26] for PV systems. When the energy supplied from the PV modules is sufficient, the converter provides energy to the DC bus while charging the battery simultaneously. However, when no energy is supplied from the PV modules, the battery can provide energy to the DC bus. A three-port DC/DC converter can operate in different modes to reduce the system's cost and size, as proposed in [24,25]. However, they have a larger system size, higher cost, and lower efficiency compared with our proposed converter topology. In general, a three-port DC/DC converter has no function of charging the battery by using the DC bus, which indicates that it lacks the step-down mode, similar to a bidirectional converter. Converters proposed in [27–29] have three operating modes, which can also use the DC bus to charge the battery. However, the count of components in [29] is higher than that of the proposed converter and the voltage gain in [28] is lower than that of the proposed converter. As proposed in [30], a three-winding common core coupled inductor was designed and implemented in the converter. If a topology can combine the advantages of bidirectional and three-port converters, the system's size and cost can be further reduced, and this was the main purpose of the present study.

This paper proposes an isolated three-port bidirectional DC/DC converter, the block diagram of which is shown in Figure 2. When the energy supplied from the PV modules is sufficient, the converter can step-up the output of the PV modules and provide energy to the DC bus while charging the battery. However, when the energy supplied from the PV modules is insufficient, the converter can step-up the output of the battery and provide energy to the DC bus. If there is excess energy in the DC bus, it will be used to charge the battery, which means that this topology can run both high-step-up and high-step-down functions.

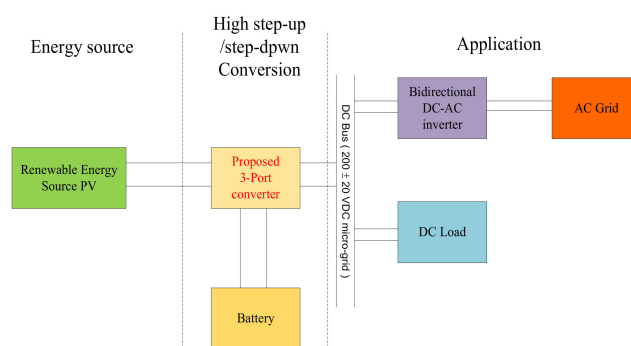


Figure 2. Block diagram of three-port bidirectional converter.

2. Circuit Architecture and Operational Principle

This paper proposes a novel three-port high-step-up/step-down bidirectional DC/DC converter with a coupled inductor, as shown in Figure 3. The DC-blocking capacitor C_m at the high-voltage side enables the system to operate in the high-step-down mode by reducing the voltage on the transformer. Moreover, synchronous rectification is performed in the switch during the high-step-up mode to reduce switch loss to increase the system's overall efficiency. Moreover, the energy stored in the leakage inductor on the transformer's secondary side can be recycled, which increases the system efficiency. An improved SEPIC is used on the low-voltage side of the PV modules to step-up the output of the PV modules for battery charging and provide energy to the DC bus. The auxiliary inductor L_b, L_1 at the battery side can modify the output step-up voltage after it is modified and provide continuous current for charging the battery. Switch S_2 and diode D_2 prevent the energy generated from the PV system from charging the battery directly and controlling the step-up process for providing energy to the DC bus and charging the battery when the energy

supplied from the PV modules is sufficient. The battery output is stepped-up and provides energy to the DC bus in case of a lack of energy supply from the PV modules. If excess energy is present in the DC bus, the energy is used to charge the battery.

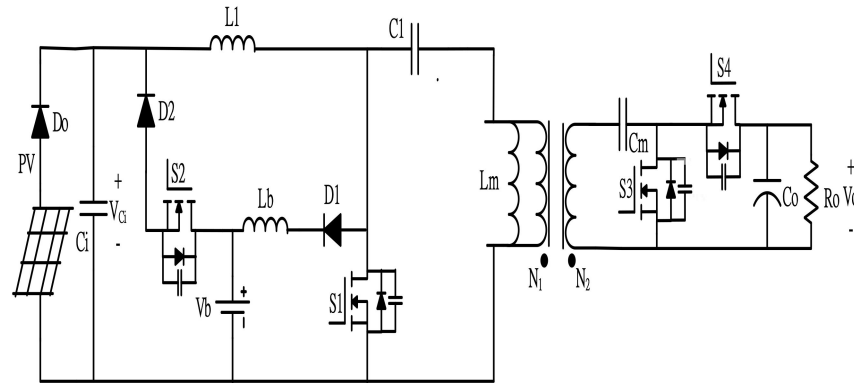


Figure 3. Novel isolated three-port bidirectional DC/DC converter.

The proposed topology can be studied in three working stages. Stage 1 involves stepping-up the output of the PV modules for charging the battery and providing energy to the DC bus when the energy supplied from the PV modules is sufficient. Stage 2 involves stepping-up the battery output to provide energy to the DC bus when the energy supplied from the PV modules is insufficient. Stage 3 involves stepping-down the output of the DC bus and charging the battery when excess energy is present in the DC bus. To simplify the analysis of the proposed topology, the following assumptions were made:

1. All the capacitances are sufficiently large and can be considered as the current sources.
2. Switches and diodes are ideal components.
3. The magnetizing inductances of the transformer are larger than its leakage inductances.

Stage 1: Step-up the PV output for the DC bus and battery charging.

The waveforms of the key components operating in Stage 1 are shown in Figure 4.

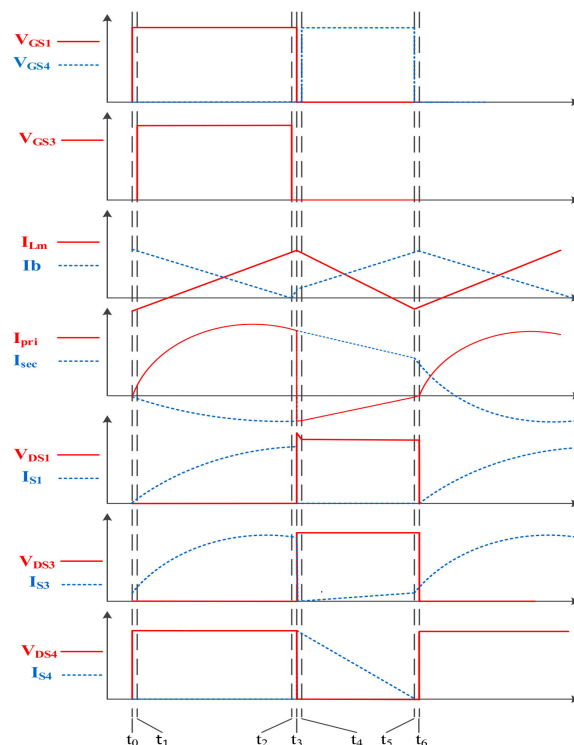


Figure 4. Key waveforms in Stage 1.

1. Mode I [$t_0 \leq t < t_1$].

As shown in Figure 5a, when $t = t_0$, switch S_1 and diode D_1 turn ON, while switches S_2, S_4 , and diode D_2 turn OFF. Furthermore, the parasitic diode of switch S_3 is turned ON, and the direction of the current flow is as shown in the figure. In this mode, the PV source stores energy in the input inductor L_1 and magnetizing inductor L_m , while the charging inductor L_b releases energy for battery charging. Simultaneously, capacitor C_1 and the current induced by the transformer are stored in the voltage-doubling capacitor C_m . During this interval, V_o is provided by the output capacitor C_o .

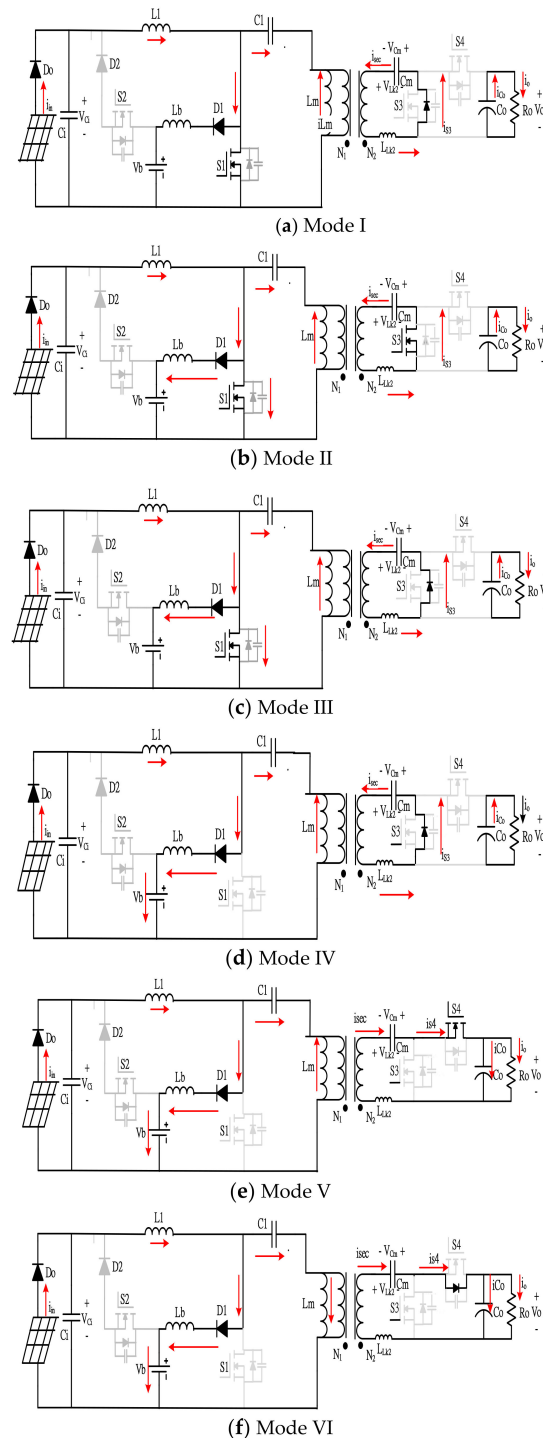


Figure 5. Operational diagram of each mode in Stage 1: (a) Mode I, (b) Mode II, (c) Mode III, (d) Mode IV, (e) Mode V, and (f) Mode VI.

2. Mode II [$t_1 \leq t < t_2$].

When $t = t_1$, S_1 and D_1 remain ON, while S_2 , S_4 , and D_2 remain OFF. In this mode, S_3 is turned ON for operating synchronous rectification, and the direction of the current flow is as shown in Figure 5b. Other operations are the same as those in Mode I. Energy is stored in L_1 and L_m by the PV source, L_b releases energy for battery charging, C_m is charged by the induced current from the transformer, and C_o continues to provide energy to the output V_o .

3. Mode III [$t_2 \leq t < t_3$].

When $t = t_2$, S_1 and D_1 still remain ON, while S_2 , S_4 , and D_2 remain OFF. The parasitic diode on S_3 is turned ON, and the direction of current flow is as shown in Figure 5c. The other operations in this mode are the same as those in Mode I.

4. Mode IV [$t_3 \leq t < t_4$].

When $t = t_3$, S_1 is turned OFF; D_1 and the parasitic diode on S_3 remain ON; S_2 , S_4 , and D_2 remain OFF. The direction of the current flow in this mode is as shown in Figure 5d. In this mode, the input inductor releases energy for charging the auxiliary inductor L_b . Moreover, the current flowing through the leakage inductor L_{Lk2} charges the parasitic capacitor, L_b releases energy for battery charging, and C_o continues to provide energy to the output V_o .

5. Mode V [$t_4 \leq t < t_5$].

When $t = t_4$, S_1 , S_2 , S_3 , and D_2 are OFF, while D_1 remains ON. Simultaneously, S_4 is turned ON for operating synchronous rectification, and the direction of the current flow is as shown in Figure 5e. In this mode, the energy stored in L_m is transferred to output V_o and charge C_o through the transformer's induction. Meanwhile, C_m releases its stored energy to the output V_o , the input inductor L_1 releases energy for charging the auxiliary inductor L_b , and L_b continues to provide energy to the battery.

6. Mode VI [$t_5 \leq t < t_6$].

When $t = t_5$, S_1 , S_2 , S_3 , and D_2 remain OFF, while D_1 remains ON. The direction of current flow in this mode is as shown in Figure 5f. Here, the parasitic diode on S_4 is turned ON, which indicates that synchronous rectification is stopped. Other operations are the same as those in Mode V.

Stage 2: Battery step-up to DC bus.

In Stage 2, the battery's output voltage is stepped-up to provide energy to the DC bus. Figure 6 shows the key waveforms of the main components operating in Stage 2.

1. Mode I [$t_0 \leq t < t_1$]

When $t = t_0$, switches S_1 and S_2 and diode D_2 turn ON, while switch S_4 and diode D_1 turn OFF. The direction of current flow in this mode is as shown in Figure 7a. In addition, the parasitic diode on S_3 is ON. In this mode, the battery releases energy to the input inductor L_1 , capacitor C_1 , and magnetizing inductor L_m . The induced current from the transformer charges the voltage-doubling capacitor C_m , while the output capacitor C_o provides energy to output V_o .

2. Mode II [$t_1 \leq t < t_2$].

During this interval, S_1 , S_2 , and D_2 remain ON, while S_4 and D_1 remain OFF. S_3 is turned ON for synchronous rectification when $t = t_1$, and the direction of current flow is as shown in Figure 7b. The other operations are the same as those in Mode I.

3. Mode III [$t_2 \leq t < t_3$].

When $t = t_3$, S_1 , S_2 , and D_2 remain ON, while S_4 and D_1 remain OFF. Simultaneously, synchronous rectification is stopped and the parasitic diode on S_3 is turned ON. The direction of current flow is as shown in Figure 7c. The other operations in this mode are the same as those in Mode I, and the battery releases energy for magnetizing inductor, L_m . The

induced current from the transformer charges the voltage-doubling capacitor C_m , while the output capacitor C_o provides energy to output V_o .

4. Mode IV [$t_3 \leq t < t_4$].

When $t = t_4$, S_1, S_2, S_3 , and D_2 remain OFF, while D_1 remains ON. Simultaneously, S_4 is turned ON to operate synchronous rectification. The direction of current flow in this mode is as shown in Figure 7e. In this mode, the transformer induces energy from L_m to output V_o while simultaneously charging C_o . The energy stored in C_m is also released to output V_o . Meanwhile, inductor L_1 releases energy for auxiliary inductor L_b charging, and the energy stored in L_m and L_b is recycled back to the battery.

5. Mode VI [$t_5 \leq t < t_6$].

When $t = t_5$, S_1, S_2, S_3 , and D_2 remain OFF, while D_1 remains ON. The synchronous rectification is stopped because the parasitic diode on S_4 is turned ON, and the direction of current flow in this mode is as shown in Figure 7f. Other operations in this mode are the same as those in Mode IV.

Stage 3: DC-bus step-down for battery charging.

When the energy supplied from the PV modules is insufficient, the system steps-down the output voltage of the DC bus for battery charging. The key waveforms of the proposed converter topology in the step-down stage are shown in Figure 8.

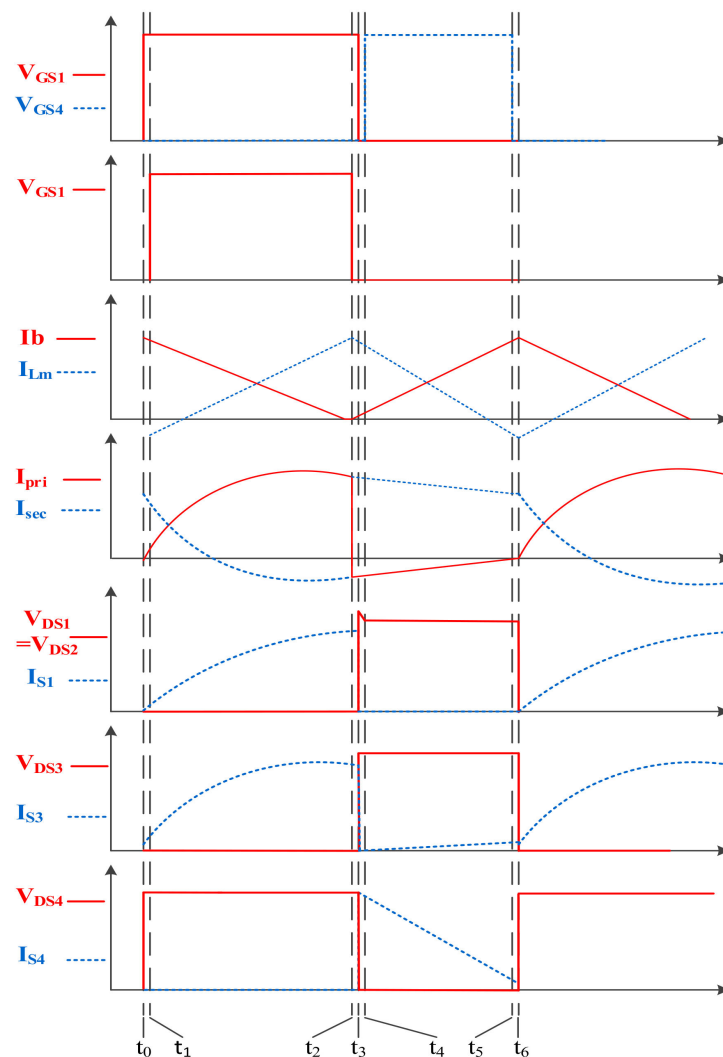


Figure 6. Key waveforms in Stage 2.

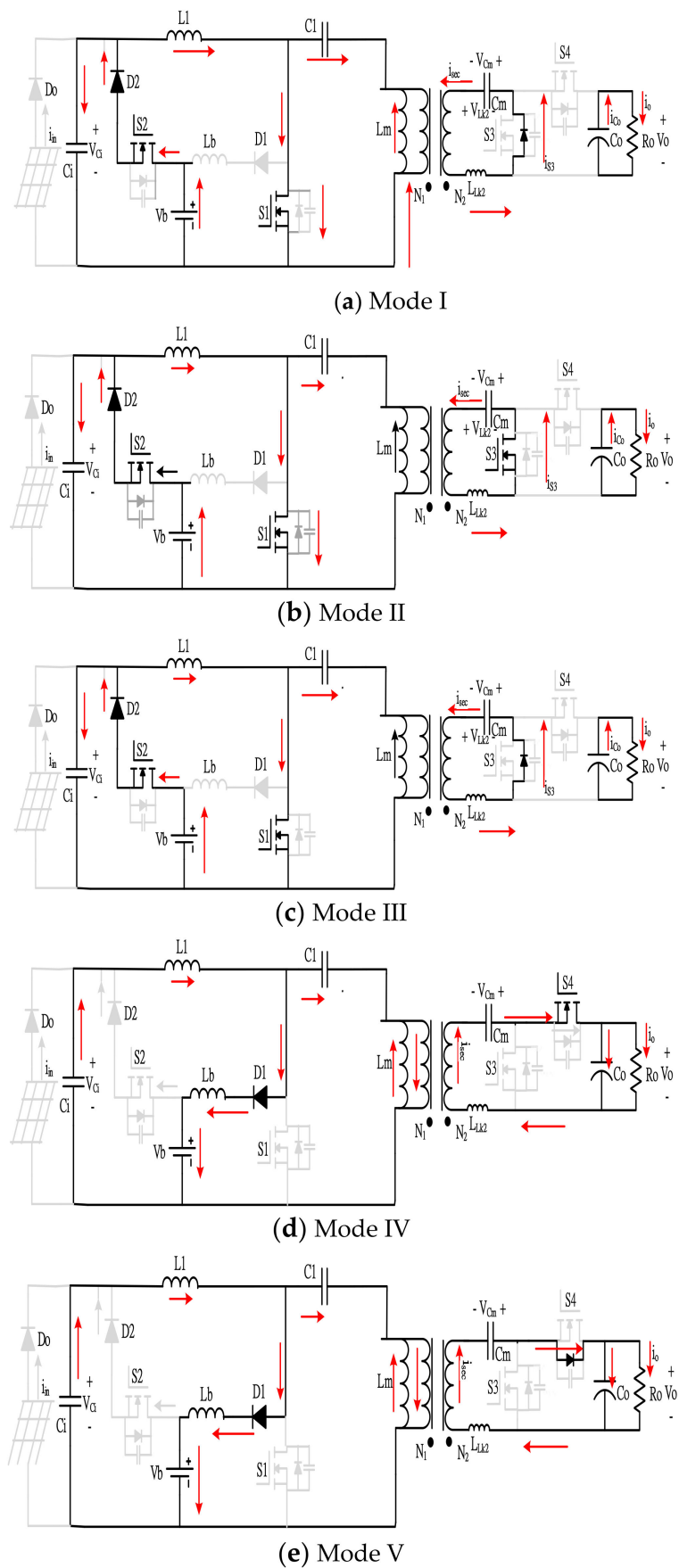


Figure 7. Operating diagram of each mode in Stage 2: (a) Mode I, (b) Mode II, (c) Mode III, (d) Mode IV, and (e) Mode V.

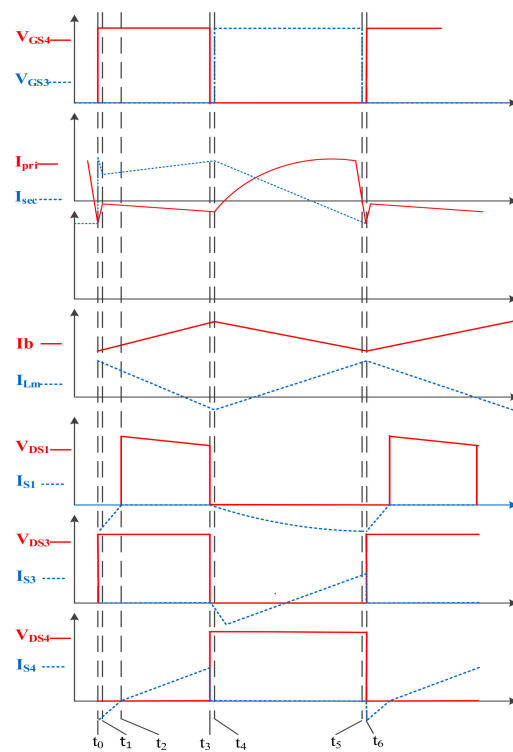


Figure 8. Key waveforms in Stage 3.

1. Mode I [$t_0 \leq t < t_1$].

When $t = t_0$, switch S_4 and diode D_1 are turned ON, while switches S_1 , S_2 , and S_3 and diode D_2 are turned OFF. Simultaneously, the parasitic diode on switch S_1 is turned ON. The direction of current flow in this mode is as shown in Figure 9a. This mode continues the state of Mode VI in Stage 2, where the energy stored in the voltage-doubling capacitor C_m and leakage inductor L_{Lk2} is recycled to output V_o , and the other leakage inductor L_{Lk1} transfers its energy to the input capacitor C_i . Simultaneously, the charging inductor L_b releases energy to charge the battery.

2. Mode II [$t_1 \leq t < t_2$].

When $t = t_1$, S_4 and D_1 remain in the ON state, while S_1 , S_2 , S_3 , and D_2 remain OFF. The direction of the current flow is shown in Figure 9b. In this mode, the PV source starts to store energy in the magnetizing inductor L_m after the energy stored in C_m and L_{Lk2} is recycled completely. In addition, the induced current from the transformer starts to store energy in L_b while simultaneously charging the battery.

3. Mode III [$t_2 \leq t < t_3$].

When $t = t_2$, S_1 , S_2 , and D_2 remain in the OFF state and D_1 remains ON. S_4 is turned OFF, while the parasitic diode on S_3 is turned ON; the direction of current flow is as shown in Figure 9c. In this mode, current flows through the leakage inductor L_{Lk2} and then charges C_m . The induced current from the transformer also stores energy in L_b while simultaneously charging the battery.

4. Mode IV [$t_3 \leq t < t_4$].

When $t = t_3$, S_2 , S_4 , and D_2 remain OFF, while D_1 remains ON. Simultaneously, both S_1 and S_3 are turned ON for operating synchronous rectification. The direction of current flow in this mode is as shown in Figure 9d. The energy stored in L_m is induced by the transformer to charge C_m through S_3 . In addition, L_b starts to release energy through S_1 while simultaneously charging the battery.

5. Mode V [$t_4 \leq t < t_5$]

When $t = t_4$, S_2 , S_4 , and D_2 remain OFF, while S_1 , S_3 , and D_1 remain ON, and the direction of current flow is as shown in Figure 9e. In this mode, both S_1 and S_3 continue to operate synchronous rectification, and the energy stored in L_m is completely released. Simultaneously, C_m starts to transfer energy to L_m and L_{Lk2} while inducing energy to charge C_j . Meanwhile, L_b continues to charge the battery through S_1 .

6. Mode VI [$t_5 \leq t < t_6$]

When $t = t_5$, D_1 remains ON, while S_3 , S_4 , and D_2 remain OFF. The direction of current flow is as shown in Figure 9f. The synchronous rectification is stopped as S_1 and S_4 are turned OFF in this mode and both their parasitic diodes are ON. The current flows through C_m and L_{Lk2} , the energy is recycled to output V_o , and the energy stored in L_b is released for battery charging.

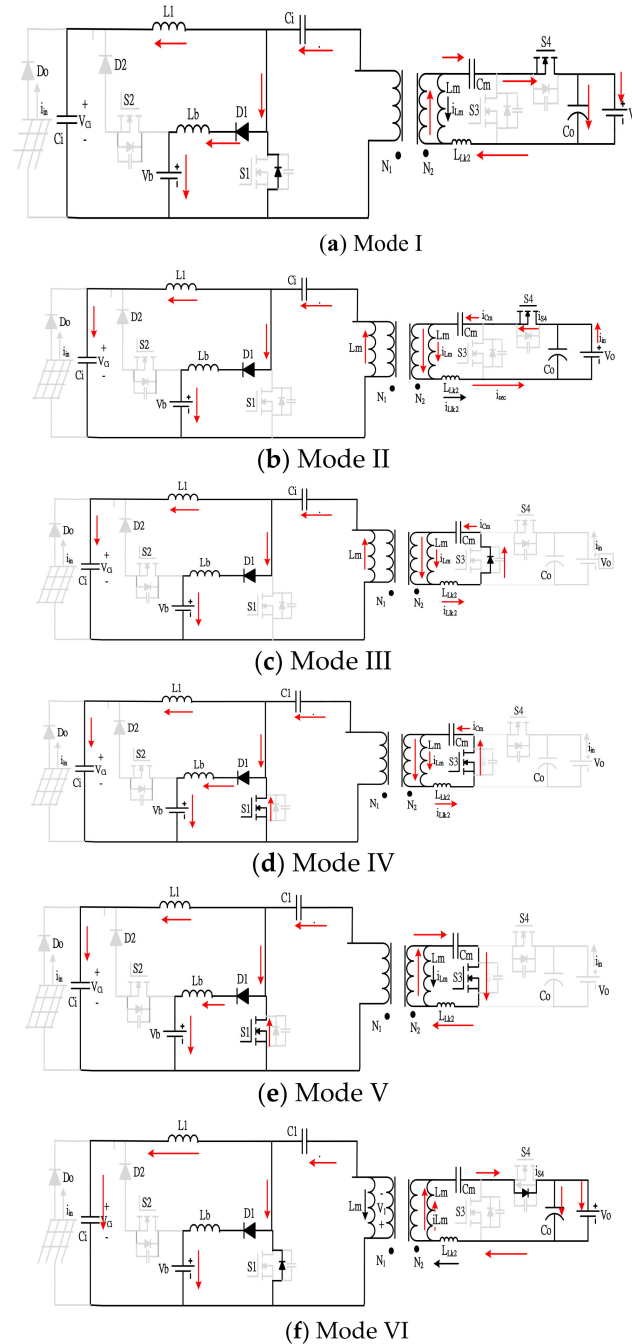


Figure 9. Operating diagram of each mode in Stage 3: (a) Mode I, (b) Mode II, (c) Mode III, (d) Mode IV, (e) Mode V, and (f) Mode VI.

3. Steady-State Analysis

This section describes the mathematical derivation of the voltage conversion ratio and the voltage stress of components. First, some assumptions are made to simplify the study and analysis process:

1. All capacitances are sufficiently large and can be considered as the current sources.
2. Switches and diodes are ideal components.
3. The leakage inductances of the transformer are smaller than the magnetizing inductances, and therefore, can be neglected.
4. The system is operating in the continuous conduction mode (CCM).

3.1. Voltage Conversion Ratio

When the energy supplied from the PV modules is sufficient, switch S_1 turns on and the voltage difference on the magnetizing inductor is equal to the input voltage supplied from the PV modules. However, when the system lacks the energy supplied from PV modules, switches S_1 and S_2 turn on and the voltage difference on the magnetizing inductor is equal to the battery voltage. Because the input voltage from the PV modules and battery voltage are almost the same in the three-port converter, both high-step-up processes of the PV modules and battery to the DC bus have the same step-up ratio. To simplify the derivation of the voltage conversion ratio, we first neglect the part of the battery circuit.

1. Step-up voltage conversion ratio, $G_{\text{step-up}}$

When switch S_1 is turned on:

$$V_{Lm} = L_m \frac{di_L}{dt} = \frac{-V_{cm}}{n} \quad (1)$$

$$\Delta i_{Lm}^+ = \frac{V_i}{L_m} DT_s \quad (2)$$

Assuming $n = \frac{N_2}{N_1}$, the total turn-on time $T_{on} = DT_s$; when switch S_1 is turned off:

$$V_L = L_m \frac{di_L}{dt} = \frac{V_o - V_{cm}}{n} \quad (3)$$

$$\Delta i_L^- = \frac{V_o - V_{cm}}{nL_m} (1 - D) T_s \quad (4)$$

Total turn-off time, $T_{off} = (1 - D) T_s$.

According to the principle of volt-second balance:

$$\Delta i_L^+ = \Delta i_L^- \quad (5)$$

$$G_{\text{step-up}} = \frac{V_o}{V_i} = \frac{n + D}{1 - D} \quad (6)$$

Assuming that all energy of the magnetizing inductors is transferred to the battery and the maximum current is equal to the stored energy current of the magnetizing inductors, we can design the battery charging current.

$$i_{Lb(\max)} = \frac{V_i}{L_m} DT_s = \frac{V_b}{L_b} DT_s \quad (7)$$

2. Step-down voltage conversion ratio, $G_{\text{step-down}}$.

For deriving the step-down voltage conversion ratio of the DC bus charging battery, switch S_2 and diode D_2 are first turned off, switch S_4 is turned on, and switch S_3 is turned off.

$$V_{Lm} = \frac{V_o - V_{cm}}{n} \quad (8)$$

$$\Delta i_{Lm} = \frac{V_o - V_{cm}}{nL_m} DT_s \quad (9)$$

Assuming $n = \frac{N_2}{N_1}$, the total turn-on time $T_{on} = DT_s$. When switch S_4 is turned off and switch S_3 is turned on:

$$V_{Lm} = \frac{-V_{cm}}{n} \quad (10)$$

$$\Delta i_{Lm} = \frac{-V_{cm}}{nL_m} (1 - D) T_s \quad (11)$$

Total turn-off time, $T_{off} = (1 - D) T_s$.

According to the principle of volt-second balance:

$$\Delta i_L^+ = \Delta i_L^- \quad (12)$$

$$G_{\text{step-down}} = \frac{V_b}{V_o} = \frac{D}{(1 - D + n)} \quad (13)$$

3.2. Voltage Stress of Components

Each component's voltage stress can be derived by analyzing their ON and OFF states. The voltage stress of switch S_1 can be determined using the ON state, as shown in Figure 5a.

$$V_i - V_{L1} = 0 \quad (14)$$

With volt-second balance, the voltage stress of switch S_1 can be derived as

$$V_{S1} = \frac{1}{1 - D} V_i \quad (15)$$

Because diode D_2 is considered ideal, the voltage of switch S_2 is equal to the voltage difference between the battery voltage and voltage on the input capacitor:

$$V_{S2} = V_b - V_{Ci} \quad (16)$$

During the step-down mode and when switch S_4 is turned ON, switch S_3 is turned OFF, as shown in Figure 9e, and the voltage difference on the switch is equal to the output voltage:

$$V_{S3} = V_o \quad (17)$$

During the step-down mode and when switch S_3 is turned ON, switch S_4 is turned OFF, as shown in Figure 9b, and the voltage difference on the switch is equal to the output voltage:

$$V_{S4} = V_o \quad (18)$$

When all the energy stored on L_b is released completely and switch S_1 is turned ON, diode D_1 is turned OFF and the voltage difference on it is equal to the battery voltage:

$$V_{D1} = V_b \quad (19)$$

Diode D_2 has the same voltage stress as that of switch S_2 .

$$V_{D2} = V_b - V_{Ci} \quad (20)$$

During the step-up mode, the voltage stress on input capacitor C_1 is expressed as

$$V_{C1} = V_{in} \quad (21)$$

The voltage stress of the output capacitor C_o is equal to V_o :

$$V_{C_o} = V_o \quad (22)$$

The voltage stress of the voltage-doubling capacitor C_m is equal to

$$V_{C_m} = V_o/2 \quad (23)$$

4. Experimental Results and Analysis

This section presents a comparison between the proposed converter and two different groups of converters. First, we compare the proposed converter with the bidirectional converter presented in [21,22]. As shown in Table 1, the converters proposed in both [21,22] can only be used as traditional bidirectional converters, whereas our three-port bidirectional converter can operate in three different stages and apply different functions. In addition to exhibiting the regular bidirectional step-up/step-down performance, our three-port bidirectional converter can be applied to the PV system. Although [20] described a clamp circuit that can reduce switch voltage stress, more components are required, and the component temperature increase causes the efficiency to decrease rapidly when operating at high wattages. Furthermore, [21] did not use any diode and reported a lower turns ratio of the transformer; it had one more inductor, which led to a larger system size. Furthermore, the efficiency in [21] obviously declined when the system operated at heavy power, and thus, the system can only operate at a maximum power of 200 W. As for [22], although the system could operate at 1 kW, its efficiency did not even reach 90% when operated above 500 W. In addition, switch controlling was very complicated.

Table 1. Comparison of the proposed converter with other presented bidirectional converters.

References	Proposed Paper	Reference [20]	Reference [21]	Reference [22]
Topology	Coupled inductor	Coupled inductor	Isolated	Isolated
Input voltage	24 V	24 V	24 V	24 V
Output voltage	200 V	400 V	200 V	200 V
Output power	500 W	500 W	200 W	1 kW
Number of Switch	4	4	4	4
Number of diode	2	0	0	2
Number of Inductor	2	2	2	1
Number of Capacitor	3	5	3	5
Turns ratio	$n = 2.5$	$n = 3$	$n = 1.5$	$n = 3$
Output terminal	2	1	1	2
Maximum conversion efficiency (Step-up/Step-down)	95.4%/94.7%	94.3%/92.6%	94%/95%	94%/95%
Cost	Medium	High	Medium	High
Converter Operational Mode	3	2	2	2

Table 2 presents a comparison between the proposed converter and those described in [24,25,28–30], all of which are three-port converters. The highest conversion efficiency shown in Table 2 is the calculated efficiency for energy conversion from PV modules to the DC bus, and the proposed converter has an obvious superiority in conversion efficiency. In addition, the proposed converter has a higher step-up ratio with fewer components and at a lower cost. The converter presented in [24] requires two coupled inductors at the output side, which results in an increased size and cost of the system. Furthermore, the power of this converter is only 150W, which will limit its application. Although the cost of the system in [25] is lower than that in [24], the system in [25] does not have an obvious superiority in terms of efficiency and system size. Moreover, it cannot reach a ten-times step-up ratio despite having the same turns ratio of the transformer as that of the transformer with the proposed converter topology. In addition, due to a lack of inductors

at the output side, the efficiency of the system decreases when operated at high power. Normally, a three-port converter cannot charge the battery by using the energy from the DC bus, but the proposed converter possesses this function, and so the proposed converter is more suitable for application to PV systems. The count of components is lowest in [28] but the voltage gain is not prominent. Moreover, the converter in [29] is nonisolated, which means that this topology is easily disturbed by noise. In industry, galvanic isolation is necessary because of safety. The number of components is too many to increase the cost, and the efficiency of the proposed converter is better than that of [29]. The performance index of [30] is moderate.

Table 2. Comparison of the proposed converter with other presented three-port converters.

References	Proposed Paper	Reference [24]	Reference [25]	Reference [28]	Reference [29]	Reference [30]
Topology	Coupled Inductor	Coupled Inductor	Isolated	Isolated	Coupled Inductor	Isolated
Input voltage	24 V	32 V	18 V	24	24–26	24–26
Battery voltage	24 V	48 V	12 V	24	24	24
Output voltage	200 V	400 V	80 V	200 V	200 V	200 V
Output power	500 W	150 W	200 W	500 W	500 W	500 W
Voltage gain of step-up mode PV-DC bus	$\frac{n+D}{1-D}$	$\frac{1+N}{1-D}$	$\frac{1}{D}$	$\frac{n}{(1-D)}$	$\frac{2+n}{1-D}$	$\frac{n}{(1-D)}$
Voltage gain of step-up mode Battery-DC bus	$\frac{n+D}{1-D}$	$\frac{1+N}{1-D}$	$\frac{1}{D}$	$\frac{n}{(1-D)}$	$\frac{2+n}{1-D}$	$\frac{n}{(1-D)}$
Voltage gain of step-down mode DC bus-battery	$\frac{D}{(1-D+n)}$	D	D	$\frac{D}{n}$	$\frac{D}{2+n}$	$\frac{(1-D)}{n}$
Number of Switch	4	4	4	4	4	4
Number of Diode	2	5	2	2	4	2
Number of Transformer	1	2	2	1	1	1
Number of Inductor	2	1	0	1	2	1
Number of Capacitor	3	5	3	3	3	3
Turns ratio	$n = 2.5$	$n = 0.5$	$n = 2$	$n=3$	$n=1$	$n=3$
Output terminal	2	2	2	2	2	2
Maximum conversion efficiency (Step-up/Step-down)	95.6%/94.5%	94.5%/93.6%	91.5%/90.6%	94.5%/95.2%	94.4%/95.0%	95%/94.2%
Converter Mode	3	3	2	3	3	3

Overall, the number of components of the proposed converter is appropriate, and the voltage gain of the proposed converter is higher. In addition, the proposed converter comes with a great performance of conversion efficiency. However, the conversion efficiency of the proposed converter still has space for improvement, if the power switch has the features of soft-switching.

To verify and demonstrate the operation of the proposed isolated bidirectional three-port DC/DC converter, a 500 W hardware prototype was designed and implemented, and the performance was measured under a full load of 500 W. Figure 10 shows the prototype of the proposed three-port bidirectional DC/DC converter. The measured waveforms of all components successfully evidenced the feasibility and practicability of the proposed converter topology. The corresponding specification and component parameters are summarized in Table 3.

Figure 11 shows the measured efficiency curve of the proposed converter topology operated under three stages. The proposed converter operates under a light load of 50 W and full load of 500 W in the PV step-up stage, with efficiencies of 93.2% and 91.4%, respectively. However, when it operates at approximately 200 W, its highest efficiency reaches 95.4%. Next, for the battery step-up stage, its highest efficiency is 94.3%. Finally, for the step-down stage, the efficiencies for the abovementioned light and full loads are

92.3% and 91.6%, respectively. However, its highest efficiency reaches 94.3% when operated at 250 W.

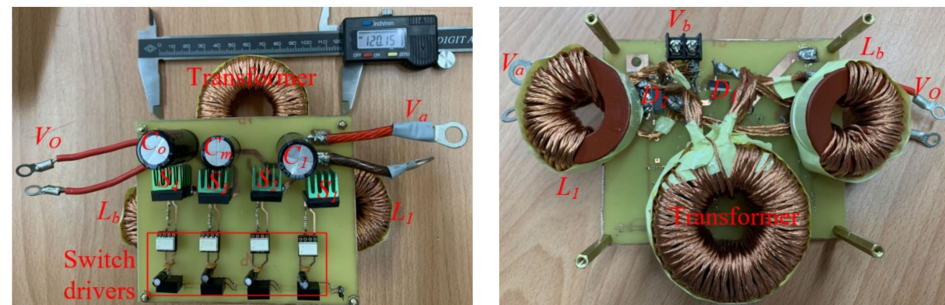


Figure 10. Photographs of the proposed three-port bidirectional DC/DC converter.

Table 3. Electrical specifications and component parameters of the proposed converter.

		Specification
Input DC Voltage V_{in}		24 V
Battery Voltage V_b		24 V
Output DC Voltage V_o		200 V
Maximum output power P_o		500 W
Switching frequency f_s		50 kHz
Coupled inductors turns ratio		$N_1:N_2 = 1:2.5$
Component	Model	Specification
S1, S2	IRFP4321	150 V/78 A
S3, S4	IRFP4868	300 V/70 A
D1, D2	MBR40200	200 V/40 A
C_i	Electrolytic Capacitor	100 μ F/100 V
C_1	Electrolytic Capacitor	220 μ F/100 V
C_o	Electrolytic Capacitor	470 μ F/450 V
C_m	MPP Film Capacitor	4.7 μ F/250 V
L_b	MPP Ring core	85 μ H
L_1	MPP Ring core	56 μ H
L_m	MPP EE core	260 μ H
L_K	Leakage inductance	0.5 μ H

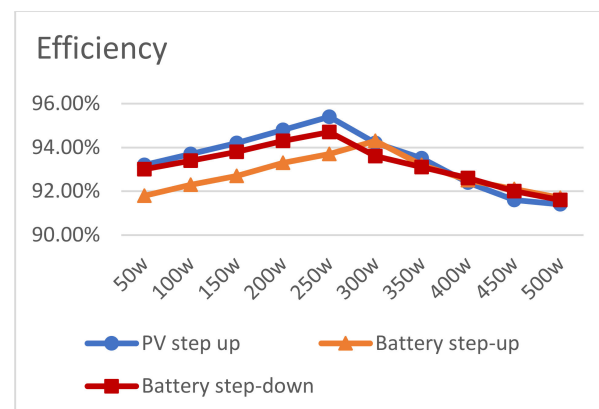


Figure 11. Efficiency curve of the proposed three-port bidirectional converter.

Figure 12 shows a comparison graph of the measured step-up efficiency between the proposed converter and those described in [20–22]. The proposed converter has a higher efficiency than those of the converters proposed in [20,22] but a lower efficiency than that proposed in [21]. However, the proposed converter can operate in three different stages and at high power. Figure 13 shows another comparison graph between the proposed converter and those described in [20,21], and Ref. [22] operated in the step-down mode. The proposed converter has a higher efficiency than the converter proposed in [20] but a lower efficiency than those proposed in [21,22]. However, the proposed converter can operate in three stages and has a low cost.

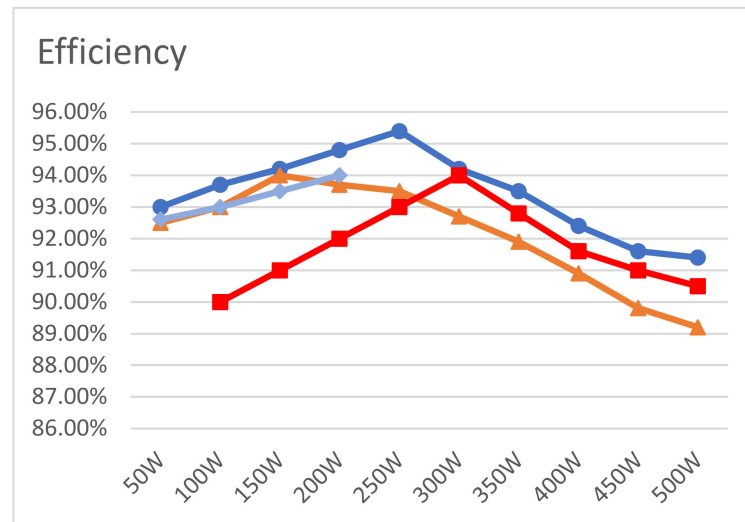


Figure 12. Comparison graph of the measured efficiency between the proposed converter and previous studies operated in the step-up mode (—●— proposed paper, —▲— [20], —◆— [21], —■— [22]).

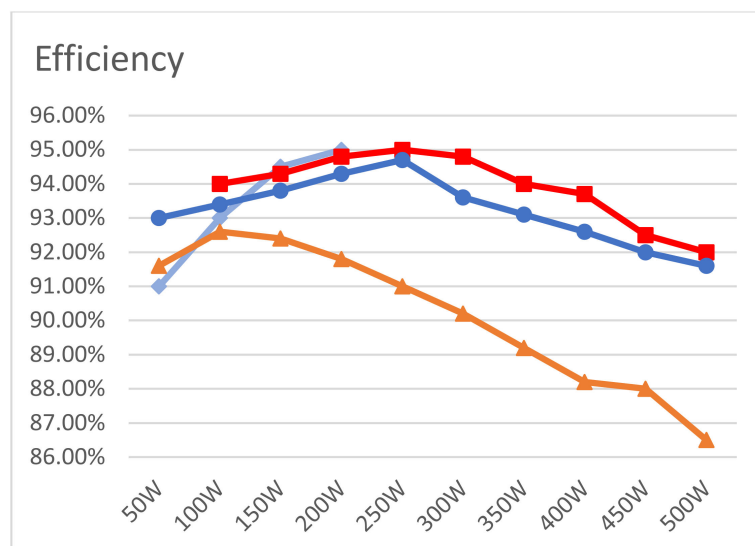


Figure 13. Comparison graph of the measured efficiency between the proposed converter and previous studies operated in the step-down mode (—◆— proposed paper, —■— [22], —●— [21], —▲— [20]).

Figure 14 shows a comparison graph of efficiency between the proposed converter and those proposed in [24,25,28,29] when operated in the PV step-up stage. The proposed converter topology has an obvious superiority over the others.

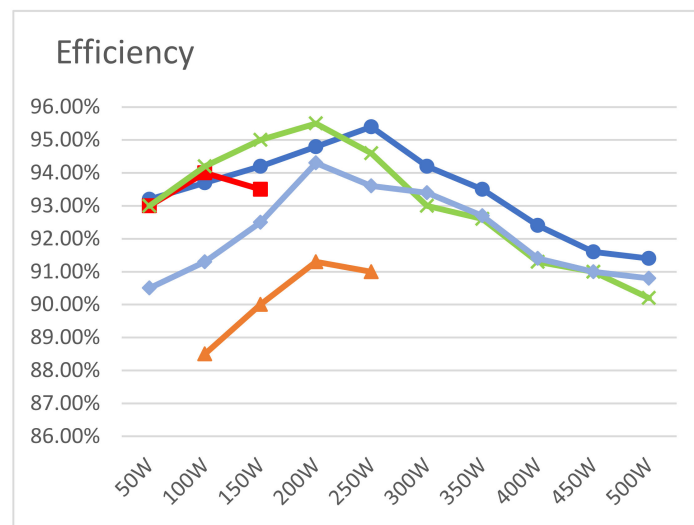
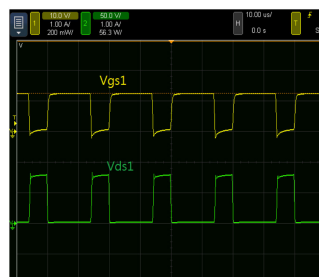
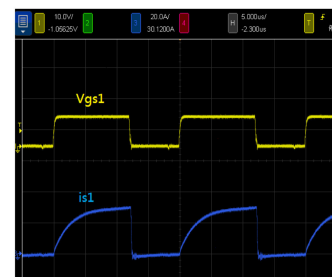


Figure 14. Comparison graph of the measured efficiency between the proposed three-port converter and previous studies (—●— proposed paper, —■— [24], —▲— [25], —×— [28], —◆— [29]).

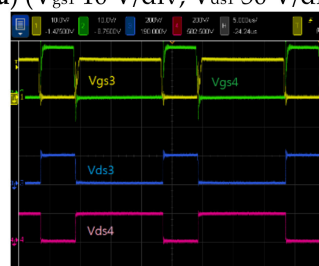
Figure 15 shows the measured results of the proposed converter under Stage 1. Figure 14a–d show the waveforms of the drive signal V_{gs} , switch voltage V_{ds} , and switch current i_s of switches S_1 , S_3 , and S_4 under a full load of 500 W, whereas the current waveforms of transformers, i_{pri} , i_{sec} , and inductors, i_{Lb} , i_{L1} , under the same load are shown in Figure 14e,f, respectively.



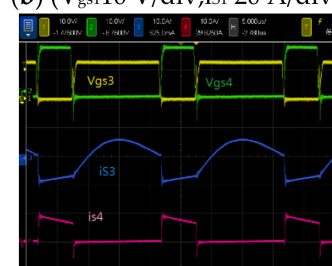
(a) (V_{gs1} 10 V/div; V_{ds1} 50 V/div)



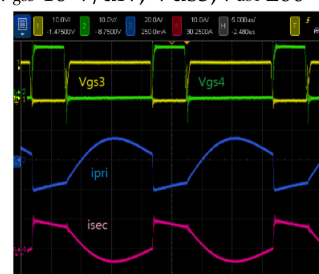
(b) (V_{gs1} 10 V/div; i_{s1} 20 A/div)



(c) (V_{gs3} 10 V/div; $V_{ds3}; V_{ds4}$ 200 V/div)



(d) (V_{gs3} 10 V/div; i_{s3} 10 A/div; i_{s4} 10 A/div)



(e) (V_{gs3} 10 V/div; i_{pri} 20 A/div; i_{sec} 10 A/div)



(f) (V_{gs3} 10 V/div; i_L 10 A/div; i_b 5 A/div)

Figure 15. Measured results under Stage 1 at 500 W: (a,b) switch S_1 waveforms, (c,d) switches S_3 and S_4 waveforms, and (e,f) current waveforms of transformers and inductors, respectively.

Figure 16 shows the measured results of the proposed converter under Stage 2. Figure 15a–d show the waveforms of the drive signal V_{gs} , switch voltage V_{ds} , and switch current i_s of switches S_1 , S_2 , S_3 , and S_4 under a full load of 500 W. Furthermore, Figure 15e,f show the current waveforms of transformers, i_{pri} , i_{sec} , and inductors, i_{Lb} , i_{L1} , under the full load, respectively.

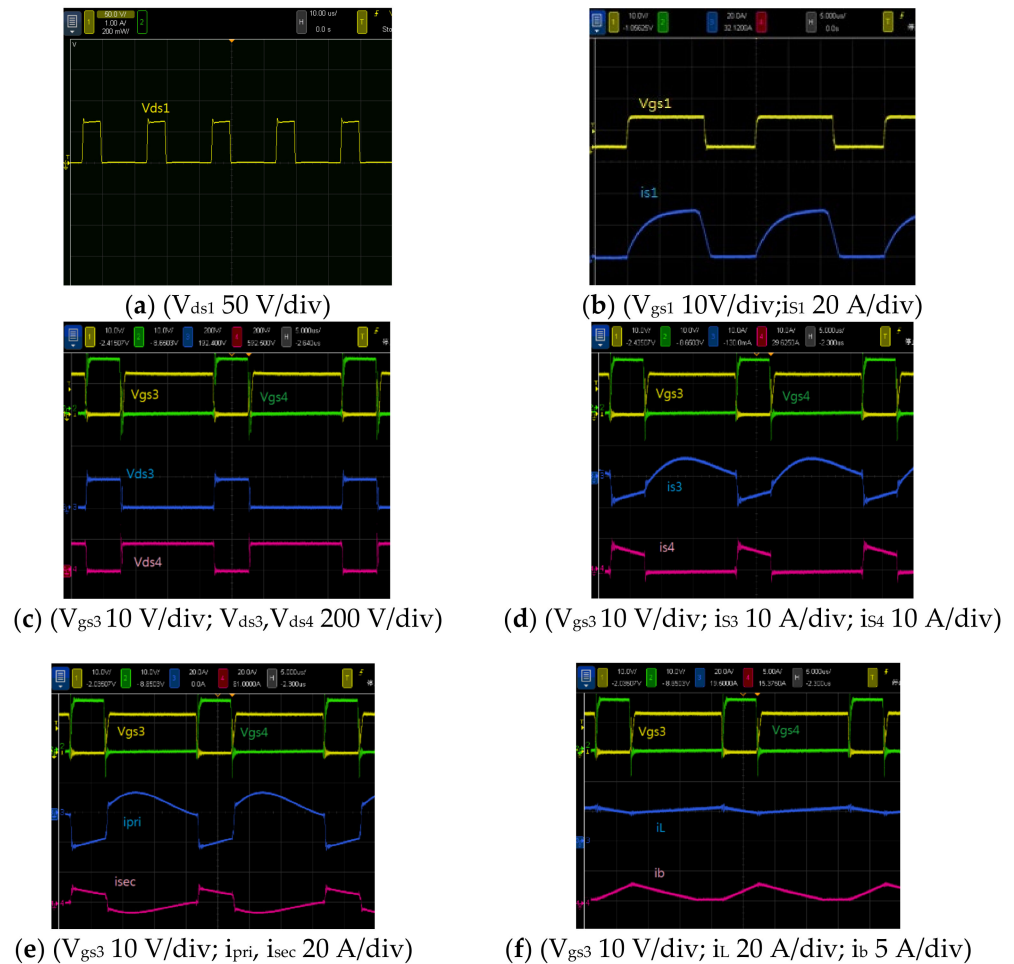


Figure 16. Measured results under Stage 2 at 500 W: (a,b) switch S_1 waveforms, (c,d) switches S_3 and S_4 waveforms, and (e,f) current waveforms of transformers and inductors, respectively.

Figure 17 shows the measured results of the proposed converter under Stage 3. Figure 16a–d show the waveforms of the drive signal V_{gs} , switch voltage V_{ds} , and switch current i_s of switches S_1 , S_3 , and S_4 under a full load of 500 W, whereas the current waveforms of transformers, i_{pri} , i_{sec} , and inductors, i_{Lb} , i_{L1} , under the same load are shown in Figure 16e,f, respectively.

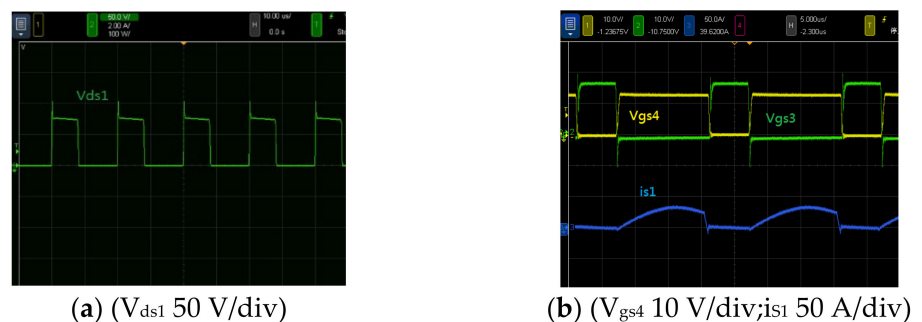


Figure 17. Cont.

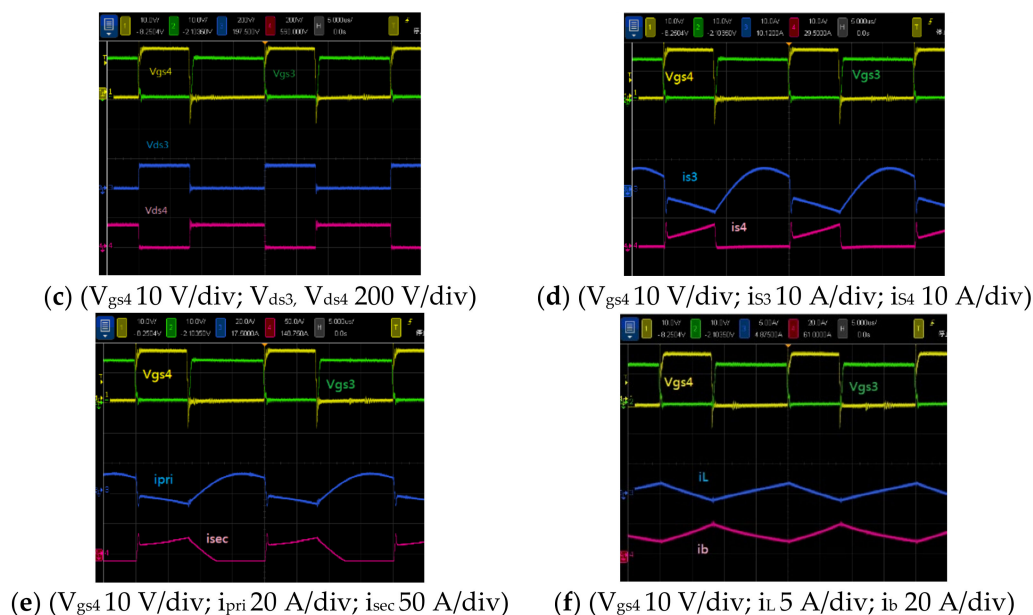


Figure 17. Measured results under Stage 3 at 500 W: (a,b) switch S_1 waveforms, (c,d) switches S_3 and S_4 waveforms, and (e,f) current waveforms of transformers and inductors, respectively.

5. Conclusions

This paper presented a theoretical analysis of the steady state, related considerations, and experimental results of the proposed converter. The proposed novel three-port high-step-up/step-down bidirectional DC/DC converter with a coupled inductor was successfully implemented. The converter possessed the PV step-up mode, battery step-up mode, and DC bus step-down mode to promote the functionality of the circuit. Moreover, an improved SEPIC and a DC-blocking capacitor were employed at the low- and high-voltage side, respectively, to promote the voltage conversion ratio and reduce the voltage of the transformer, which allows a high-step-down performance. In addition, the energy stored in the leakage inductor was recycled, which improved the system's overall efficiency. Thus, the proposed converter possessed the advantages of high efficiency, high-step-up/down ratio, and lower system size and cost. Finally, a 500 W three-port bidirectional converter was implemented to verify its feasibility and practicability. The highest efficiency of the proposed converter operated under the PV step-up stage was 95.4%, that under the battery step-up stage was 94.3%, and that under the step-down stage was 94.7%. Three-port bidirectional converters can be widely used in smart grid systems, energy storage systems, and electric vehicle power supply systems in the future.

Funding: This research received no external funding.

Institutional Review Board Statement: Not applicable.

Informed Consent Statement: Not applicable.

Data Availability Statement: Not applicable.

Conflicts of Interest: The authors declare no conflict of interest.

References

1. Facing Global Warming—Taiwan's Response. Response to the Framework Convention on Climate Change News in Taiwan. Available online: <http://www.tri.org.tw/unfccc/> (accessed on 12 May 2021).
2. Ministry of Economic Affairs Bureau of Energy. 2017 Energy and Industrial Technology White Paper. Available online: https://www.moeaboe.gov.tw/ECW/populace/content/ContentDesc.aspx?menu_id=5494 (accessed on 12 May 2021).
3. Ismail, E.H.; Al-Saffar, M.A.; Sabzali, A.J. High Conversion Ratio DC-DC Converters with Reduced Switch Stress. *IEEE Trans. Circuits Syst. I* **2008**, *55*, 2139–2151. [[CrossRef](#)]

4. Wuhua, L.; Xiaodong, L.; Deng, Y.; Liu, J.; He, X. A Review of Non-Isolated High Step-Up DC/DC Converter in Renewable Energy Applications. In Proceedings of the Applied Power Electronics Conference and Exposition, 2009, APEC 2009, Washington, DC, USA, 15–19 February 2009; 2009; pp. 364–369.
5. Dimna Denny, C.; Shahin, M. Analysis of bidirectional SEPIC/Zeta converter with coupled inductor. In Proceedings of the 2015 International Conference on Advancements in Power and Energy (TAP Energy), Kollam, India, 24–26 June 2015; pp. 103–108.
6. Zhao, Q.; Lee, F.C. High Performance Coupled-Inductor DC-DC Converters. In Proceedings of the IEEE APEC Conference, Miami Beach, FL, USA, 9–13 February 2003; Volume 1, pp. 109–113.
7. Huber, L.; Jovanovic, M.M. A design approach for server power supplies for networking applications. In Proceedings of the IEEE INTELEC, Phoenix, AZ, USA, 10–14 September 2000; pp. 1163–1169.
8. Feng, X.G.; Liu, J.J.; Lee, F.C. Impedance specifications for stable DC distributed power systems. *IEEE Trans. Power Electron.* **2002**, *17*, 157–162. [[CrossRef](#)]
9. Wu, T.F.; Yu, T.H. Unified approach to developing single-stage power converters. *IEEE Trans. Aerosp. Electron. Syst.* **1998**, *34*, 211–223.
10. Luo, F.L.; Ye, H. Positive output super-Lift converters. *IEEE Trans. Power Electron.* **2003**, *18*, 105–113.
11. Zhao, Q.; Tao, F.; Lee, F.C. A Front-end DC/DC Converter for Network Server Applications. In Proceedings of the IEEE PESC Conference, Vancouver, BC, Canada, 17–21 June 2001; Volume 3, pp. 1535–1539.
12. Wai, R.J.; Duan, R.Y. High step-up converter with coupled-inductor. *IEEE Trans. Power Electron.* **2005**, *20*, 1025–1035. [[CrossRef](#)]
13. Hassan, W.; Soon, J.L.; Lu, D.D.; Xiao, W. A High Conversion Ratio and High-Efficiency Bidirectional DC–DC Converter with Reduced Voltage Stress. *IEEE Trans. Power Electron.* **2020**, *35*, 11828–11831. [[CrossRef](#)]
14. Zhang, Y.; Liu, Q.; Li, J.; Sumner, M. A Common Ground Switched-Quasi-Z-Source Bidirectional DC–DC Converter with Wide-Voltage-Gain Range for EVs With Hybrid Energy Sources. *IEEE Trans. Ind. Electron.* **2018**, *65*, 5189–5191. [[CrossRef](#)]
15. Gorji, S.A.; Sahebi, H.G.; Ektesabi, M.; Rad, A.B. Topologies and Control Schemes of Bidirectional DC–DC Power Converters: An Overview. *IEEE Access* **2019**, *7*, 118002–118003. [[CrossRef](#)]
16. Mukhtar, N.M.; Lu, D.D. A Bidirectional Two-Switch Flyback Converter with Cross-Coupled LCD Snubbers for Minimizing Circulating Current. *IEEE Trans. Ind. Electron.* **2019**, *66*, 5948–5957. [[CrossRef](#)]
17. Bai, C.; Han, B.; Kwon, B.; Kim, M. Highly Efficient Bidirectional Series-Resonant DC/DC Converter Over Wide Range of Battery Voltages. *IEEE Trans. Power Electron.* **2020**, *35*, 3636–3650. [[CrossRef](#)]
18. Shi, H.; Sun, K.; Wu, H.; Li, Y. A Unified State-Space Modeling Method for a Phase-Shift Controlled Bidirectional Dual-Active Half-Bridge Converter. *IEEE Trans. Power Electron.* **2020**, *35*, 3254–3265. [[CrossRef](#)]
19. Haneda, R.; Akagi, H. Design and Performance of the 850-V 100-kW 16-kHz Bidirectional Isolated DC–DC Converter Using SiC-MOSFET/SBD H-Bridge Modules. *IEEE Trans. Power Electron.* **2020**, *35*, 10013–10025. [[CrossRef](#)]
20. Wu, H.; Sun, K.; Chen, L.; Zhu, L.; Xing, Y. High Step-Up/Step-Down Soft-Switching Bidirectional DC–DC Converter with Coupled-Inductor and Voltage Matching Control for Energy Storage Systems. *IEEE Trans. Ind. Electron.* **2016**, *63*, 2892–2903. [[CrossRef](#)]
21. Lee, H.-Y.; Liang, T.-J.; Chen, J.-F.; Chen, K.-H. Design and Implementation of a Bidirectional SEPIC-Zeta DC-DC Converter. In Proceedings of the 2014 IEEE International Symposium on Circuits and Systems (ISCAS), Melbourne, Australia, 1–5 June 2015; pp. 101–104.
22. Liang, T.-J.; Lee, J.-H. Novel High-Conversion-Ratio High-Efficiency Isolated Bidirectional DC–DC Converter. *IEEE Trans. Ind. Electron.* **2015**, *62*, 4492–4503. [[CrossRef](#)]
23. Wai, R.-J.; Liaw, J.-J. High-Efficiency-Isolated Single-Input Multiple-Output Bidirectional Converter. *IEEE Trans. Power Electron.* **2015**, *30*, 4914–4930. [[CrossRef](#)]
24. Faraji, R.; Farzanehfard, H. Soft-switched nonisolated high step-up three-port DC–DC converter for hybrid energy systems. *IEEE Trans. Power Electron.* **2018**, *33*, 10101–10111. [[CrossRef](#)]
25. Li, W.; Xu, C.; Luo, H.; Hu, Y.; He, X.; Xia, C. Decoupling-Controlled Triport Compositated DC/DC Converter for Multiple Energy Interface. *IEEE Trans. Ind. Electron.* **2015**, *62*, 4504–4513. [[CrossRef](#)]
26. Hu, Y.; Xiao, W.; Cao, W.; Ji, B.; Morrow, D.J. Three-Port DC–DC Converter for Stand-Alone Photovoltaic Systems. *IEEE Trans. Power Electron.* **2015**, *30*, 3068–3076. [[CrossRef](#)]
27. Wu, Y.-E. Novel High Efficiency Three-Port Bidirectional Step-up/Step-down DC/DC Converter for Photovoltaic Systems. In Proceedings of the 2020 IEEE 3rd International Conference on Electronics Technology, Chengdu, China, 8–11 May 2020; pp. 289–296.
28. Wu, Y.-E.; Chiu, P.-N. A High-Efficiency Isolated-Type Three-Port Bidirectional DC/DC Converter for Photovoltaic Systems. *Energies* **2017**, *10*, 434. [[CrossRef](#)]
29. Wu, Y.-E.; Hsiao, S.-L. Novel High-Efficiency Three-Port Bidirectional Step-up/Step-down DC–DC Converter for Photovoltaic Systems. *Sustainability* **2021**, *13*, 7913. [[CrossRef](#)]
30. Wu, Y.-E.; Hsu, K.-C. Novel Three-Port Bidirectional DC/DC Converter with Three-Winding Coupled Inductor for Photovoltaic System. *Energies* **2020**, *13*, 1132. [[CrossRef](#)]